

## Study on seismic performance of suspended ceiling system with semi-free boundary condition

Yong Wang<sup>a,b,c</sup>, Huanjun Jiang<sup>a,b,\*</sup>, Shojiro Motoyui<sup>d</sup>, Kazuhiko Kasai<sup>e</sup>, Zhiyuan Qin<sup>f</sup>, Youlu Huang<sup>a,b</sup>

<sup>a</sup> State Key Laboratory of Disaster Reduction in Civil Engineering, Tongji University, Shanghai, China

<sup>b</sup> International Joint Research Laboratory of Earthquake Engineering, Tongji University, Shanghai, China

<sup>c</sup> China State Construction Engineering Co., Ltd., Beijing, China

<sup>d</sup> School of Environment and Society, Tokyo Institute of Technology, Yokohama, Japan

<sup>e</sup> Institute of Innovative Research, Tokyo Institute of Technology, Yokohama, Japan

<sup>f</sup> College of Engineering, Computing and Applied Science, Clemson University, Clemson, SC, USA



### ARTICLE INFO

**Keywords:**

Suspended ceiling system  
Semi-free boundary condition  
Seismic performance  
Shaking table test  
Numerical simulation

### ABSTRACT

The failure of suspended ceiling system (SCS) has been one of the most widely reported seismic damage to non-structural components in buildings in recent years. In China, there are several types of SCSs applied in practice, among which the double-layer SCS with mineral wool boards is widely used in public buildings. It was found from the past earthquakes that the ceiling perimeter is one of the most vulnerable parts of SCS due to lack of reliable connection at the boundary. In this study a new semi-free boundary condition is proposed to improve the seismic performance of SCS. The full-scale shaking table tests on this type of SCS installed on a steel platform are conducted. The working mechanism, failure patterns, damage evolution, and earthquake responses including acceleration, displacement, and strain responses are studied. Experimental results verify that the proposed boundary condition is able to protect the ceiling perimeter from damage. The failure of SCS is mainly caused by the high vulnerability of grid connections. The pounding at the perimeter of SCS affects the seismic performance of the SCS harmfully. Effective seismic measures should be developed to reduce the impact between the ceiling and surroundings. A simplified numerical model for SCS with semi-free boundary condition is developed using OpenSEES. The calculated acceleration and displacement responses agree well with the test results. Moreover, seismic design recommendations for the type of SCS are provided.

### 1. Introduction

During moderate or strong earthquakes in recent years, the damage to non-structural components (NSCs) leads to great property loss, interruption of building function, and even threat to life safety although the main building structures suffer minor damage [1–4]. As one of the most popular NSCs in buildings, the suspended ceiling system (SCS) with mineral wool boards suffers serious damage during earthquakes. The common types of damage to SCS with mineral wool boards include dislodgement and falling of ceiling panels, unseating of ceiling grid members around the perimeter, buckling and failure of ceiling grid connections, buckling of ceiling grid members, failure of supporting elements, and the collapse of ceilings [5]. Among all the above damage patterns, the ceiling perimeter is regarded as one of the most vulnerable

parts of SCS. This is especially true for the SCS with mineral wool boards applied in China, which lacks reliable connection at the boundary, easily causing the falling of the gird members near the ceiling perimeter from the support and even further triggering continuous collapse of the ceiling during earthquakes.

For the SCSs with mineral wool boards around the world, there are four main types of typical boundary condition for the ceiling perimeter: free, fixed, fixed-free, and fixed-semi-free. The SCS with the free boundary condition (Fig. 1a) refers to the SCS which is placed on the peripheral support without any attachments connected with the surroundings so that at the boundary the SCS moves freely in the horizontal direction except the constraint due to the friction (Fig. 2a). The SCS with the free boundary condition is generally applied in areas with light to moderate earthquake potential (Seismic Design Category C) according

\* Corresponding author at: State Key Laboratory of Disaster Reduction in Civil Engineering, Tongji University, Shanghai 200092, China.  
E-mail address: [jhj73@tongji.edu.cn](mailto:jhj73@tongji.edu.cn) (H. Jiang).

to current American standards [6]. This type of SCS is required to have a minimum 10 mm gap between the grid end and wall angle on all boundaries to accommodate the movement of SCS relative to the main structure during earthquakes. In some countries including China, the SCS with free boundary condition is used extensively in practice due to the ease of its construction. In this type of SCS, the boundary constraints on the different sides are identical. That is, the boundary constraint effect is uncoupled for this type of SCS. Since this type of SCS has weak boundary constraint, it is prone to collide with the surroundings under the earthquake, which often leads to serious damage to the ceiling perimeter.

The SCS with the fixed boundary condition (Fig. 1b) refers to the SCS which is fixed to the surroundings on all sides of the perimeter. Two common types of peripheral fixings currently are applied in practice, namely pop rivets and seismic clips. Two types of tests, system-level shaking table tests [7–11] and component-level static tests [12–15], were performed to investigate the seismic performance of the fixed connections with pop rivets (Fig. 2b). Although the pop rivet could somewhat improve the seismic capacity of the ceiling perimeter, the early failure of pop rivet often occurs when the forces acting on it exceed the shear strength of the pop rivet. Moreover, the installation of pop rivets at the perimeter of the ceiling may lead to the aesthetic problem. As an alternative solution to these issues, seismic clips are adopted to be attached at the grid ends beside wall angles. To evaluate the seismic capacity of the fixed connections with seismic clips (Fig. 2c), extensive experimental tests including component-level [12–13,15] and system-level [8–11,16] tests were conducted. Compared with the connection with pop rivets, the connection with seismic clips installed with perimeter screws at the fixed side with larger strength and deformability considerably improve the seismic behavior of ceiling perimeter.

Although compared with the free boundary condition, the fixed boundary condition can significantly enhance the strength and stiffness of ceiling perimeter, the stronger boundary constraint allows inertia forces induced in SCS to transfer and accumulate at the peripheral fixings, making these peripheral connections the most vulnerable components of SCS.

The SCS with the fixed-free boundary condition (Fig. 1c) refers to the SCS which is fixed to the surroundings at two adjacent sides of the perimeter, and placed on the peripheral support with a minimum 19 mm gap between the grid end and wall angle to allow the free movement of the grid on the opposite two sides. The different boundary constraint effect is coupled in the SCS. This type of SCS, called as “American-style SCS”, is applied in buildings in high seismic zones (Seismic Design Category D-F) [6]. With the improvement of seismic clips invented by the major manufacturers in the US, the fixed-free condition is developed into fixed-semi-free boundary condition (Fig. 1d) more commonly used. The semi-free side is achieved by means of seismic clips with one sliding screw attached at the middle slot to allow the grid to slide freely only along the axis of the grid (Fig. 2d). On the semi-free side, a minimum 19 mm gap is set between the grid end and wall angle. Unfortunately, the current construction measures for fixed and semi-free connections at the boundary are inadequate, for example, the flange of seismic clip is not firmly connected to the surroundings due to the lack of sufficient perimeter screws.

In this study a new boundary condition, i.e. semi-free boundary condition, is proposed to improve the seismic performance of double-layer SCS with mineral wool boards wildly used in China. The four peripheral sides of SCS are set to be semi-free by adopting seismic clips, so there is no coupling effect of boundary constraints on the four sides for this type of SCS. Moreover, the SCS with same semi-free boundary

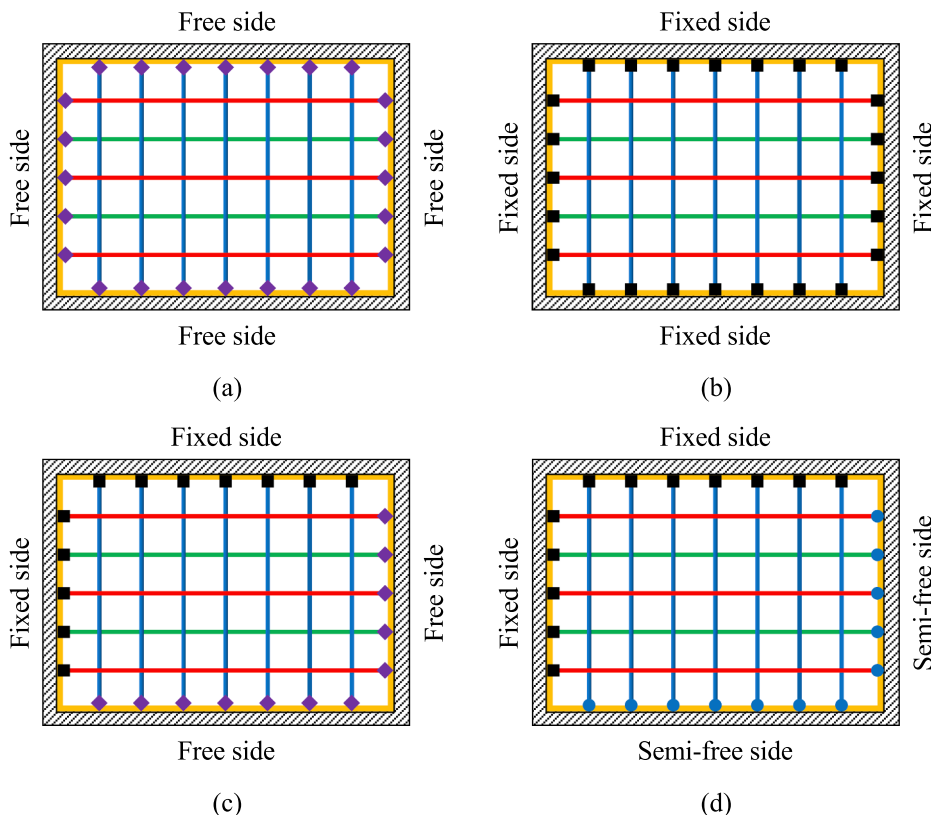


**Fig. 1.** Typical boundary condition for SCS: (a) free boundary condition, (b) fixed boundary condition, (c) fixed-free boundary condition, (d) fixed-semi-free boundary condition. Notes: — main tee; — cross tee; — sub cross tee; — wall angle; // surrounding wall; ♦ free connection; ■ fixed connection; ● semi-free connection.

condition at four sides has the advantages of clearer working mechanism and simpler numerical modeling. The seismic clip is attached tightly to the surroundings by using all available perimeter screws to improve the seismic capacity of the connection with seismic clips. The semi-free boundary condition is not only to prevent the falling of the gird members near the ceiling perimeter from the support, but also to release the boundary constraints to reduce the damage to the peripheral connections. Moreover, the proposed boundary condition has the advantages of convenient construction and low cost. To verify the working mechanism and investigate the seismic performance of the SCS with semi-free boundary condition, the full-scale shaking table tests are carried out in this study. Then, a simplified numerical model for SCS with semi-free boundary condition is proposed and verified. Finally, seismic design recommendations for the type of SCS are provided.

## 2. Semi-free boundary condition

### 2.1. Configuration

The proposed semi-free boundary condition is achieved by installing semi-free connections (SFCs) all around the ceiling perimeter. The SFC consists of perimeter grid, seismic clip, wall angle, and side wall, as shown in Fig. 3. The wall angle is fixed to the side wall using screws. The seismic clip is attached tightly to the wall angle and side wall using four perimeter screws to obtain the enough bearing capacity of SFC. The perimeter grid is connected to the seismic clip only by one sliding screw in the middle slot of the seismic clip to ensure that the perimeter grid slides freely only along its axial direction while the movement perpendicular to the axial direction of the perimeter grid is prevented. In

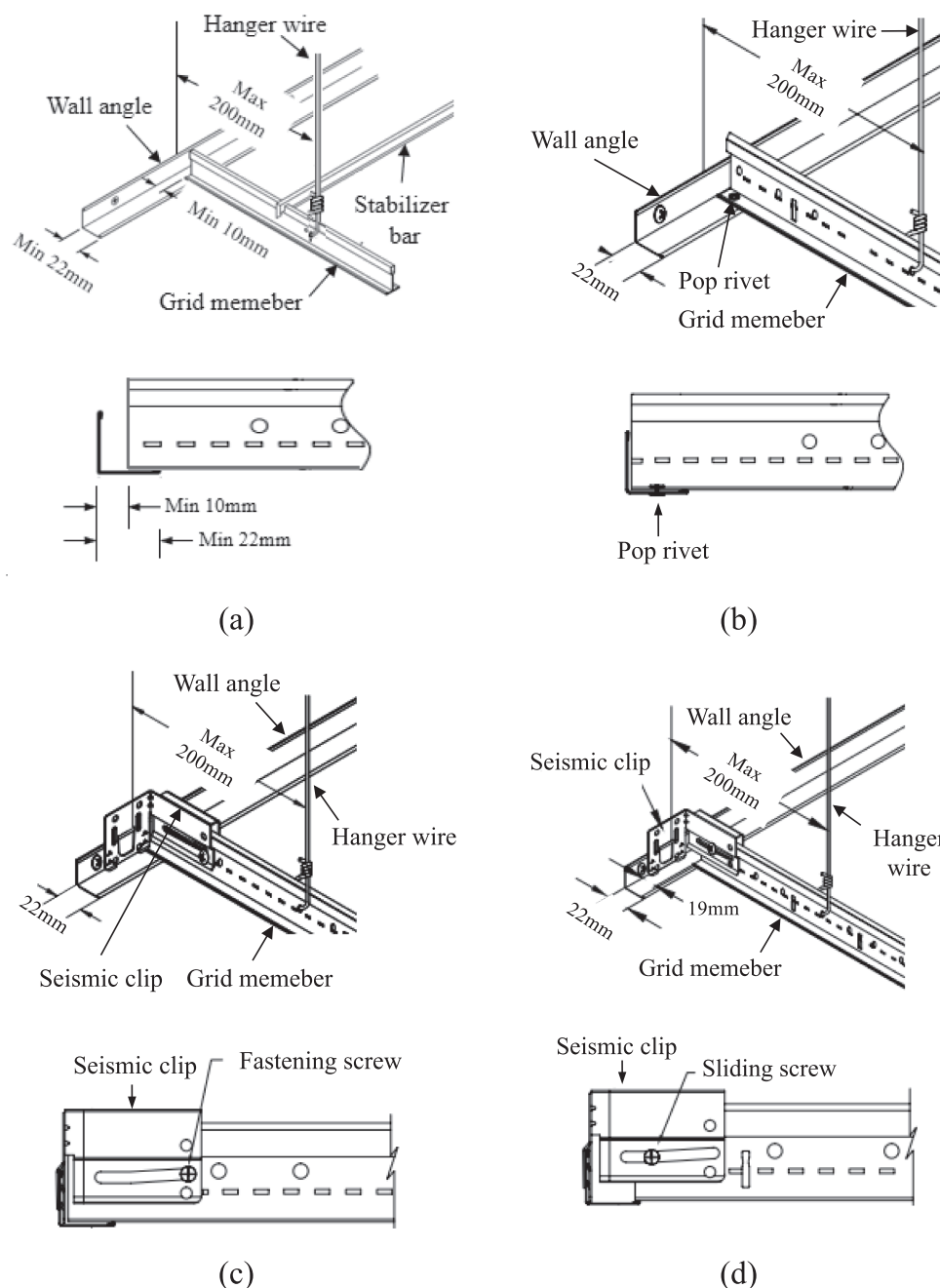


**Fig. 2.** Typical perimeter connections of SCS: (a) free connection, (b) fixed connection with pop rivet, (c) fixed connection with seismic clip, (d) semi-free connection with seismic clip.

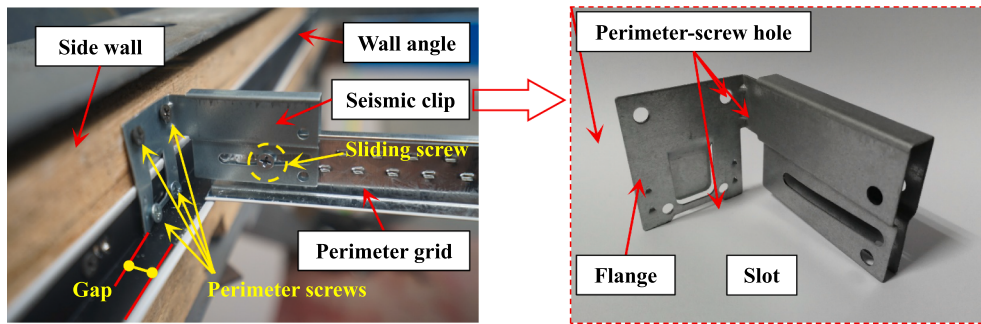


Fig. 3. Schematic of semi-free connection.

addition, a 19 mm gap is provided between the perimeter grid end and wall angle. Considering the mechanical configuration of SFC, the seismic performance of the proposed SCS is expected to be enhanced largely because of energy dissipation by the friction mechanism between middle slot and sliding screw along the axial direction of the perimeter grid, and also by the increased flexural, shear and torsional resistance perpendicular to the axial direction of the perimeter grid after the installation of seismic clips.

Fig. 4 shows a schematic view of the displacement mechanism along the longitudinal direction for SCSs with and without seismic clip connections. The movement of SCS with seismic clips is effectively constrained by seismic clips, and the flexural, shear and torsional resistance of peripheral connections is improved significantly.

## 2.2. Working mechanism

Fig. 5 shows the whole process of movement of the ceiling grid with semi-free boundary condition, which can be divided into three stages: pre-slipping, slipping, and pounding stages. The expressions of “Gap-1” and “Gap-4” refer to the gap width of 19 mm between the grid end and the wall angle. The expressions of “Gap-2”, “Gap-3”, “Gap-5”, and “Gap-6” refer to the gap width of 22 mm between the sliding screw and the edge of the middle slot of seismic clip. The sliding screw is set in the middle of the slot.

- (a) Pre-slipping stage: During the pre-slipping stage, the grid ends are restrained by the friction force which is larger than the inertial force acting on the grid. The displacement of the grid relative to the side wall is very small and close to zero, which indicates that the ceiling moves with the main structure together. The acceleration of the ceiling is close to that of the main structure.
- (b) Slipping stage: During the slipping stage, the grid end begins to slide because the inertial force acting on the grid is larger than the friction force. The displacement of the grid becomes greater but is

smaller than the gap between the grid end and wall angle. The movement process of the grid is described as follows. When the grid overcomes the friction force and moves to the left side, the left grid slides on the surface of the wall angle while the right grid slides to the left along the inclined middle slot of seismic clip and simultaneously lifts off from the surface of the wall angle. No pounding occurs since the displacement of the grid end relative to the side wall is less than Gap-1. Similarly, when the grid moves to the right side, no pounding occurs. It should be noted that when the grid moves to the right side, the right grid end will return to the surface of the wall angle and slide on the wall angle.

- (c) Pounding stage: During the pounding stage, the grid end collides with the wall angle because the displacement of the grid end relative to the side wall is greater than Gap-1. The grid acceleration response increases significantly, and the inertial force acting on the grid is larger than the friction force at the grid end. The movement process of the grid is described as follows. Firstly, the grid experiences the slipping stage. Then, when the grid moves to the left side after the slipping stage, the location of pounding is determined by the smallest gap among Gap-1, Gap-2, and Gap-6. In the case that Gap-1 is the smallest, the pounding occurs between the left grid end and wall angle. The pounding force acting on the grid end is significant. Similarly, when the grid moves to the right side, the pounding occurs between the right grid end and wall angle.

## 3. Test program

### 3.1. Test setup

The full shaking table tests on the SCS with semi-free boundary condition were conducted to investigate the working mechanism, damage mechanism, and seismic responses of the SCS subjected to earthquake induced excitation. The steel platform is used as a test carrier

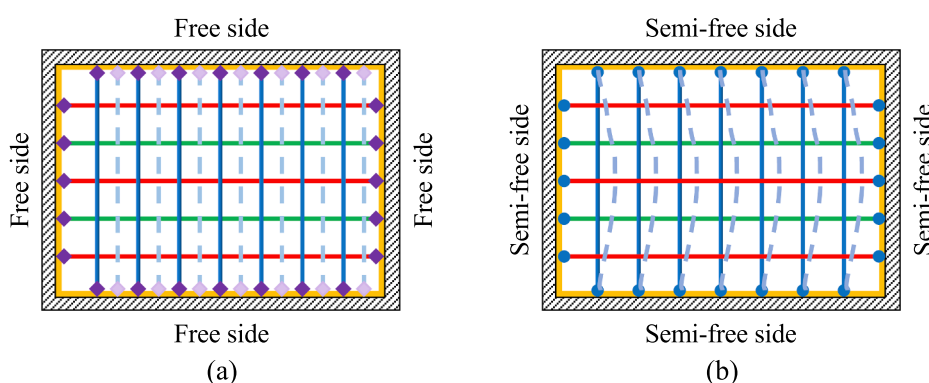
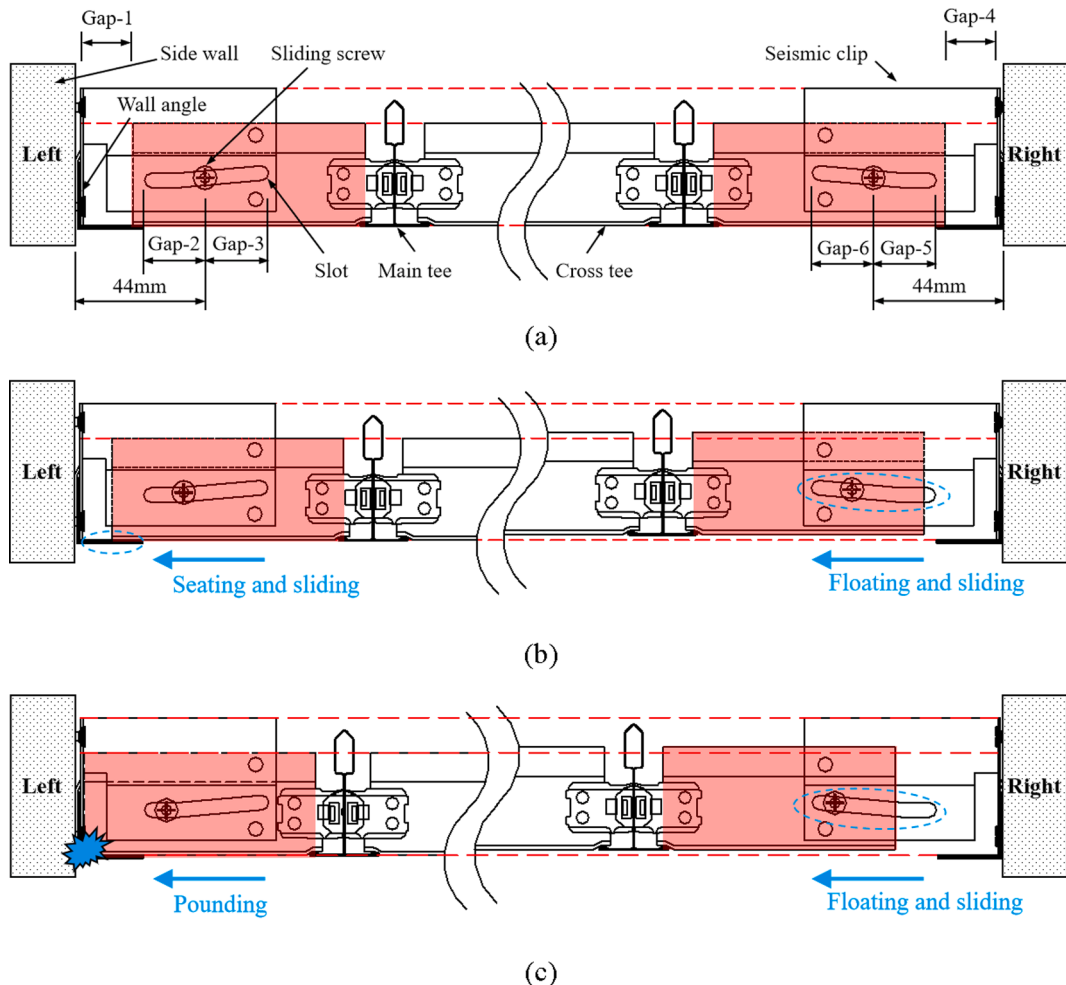
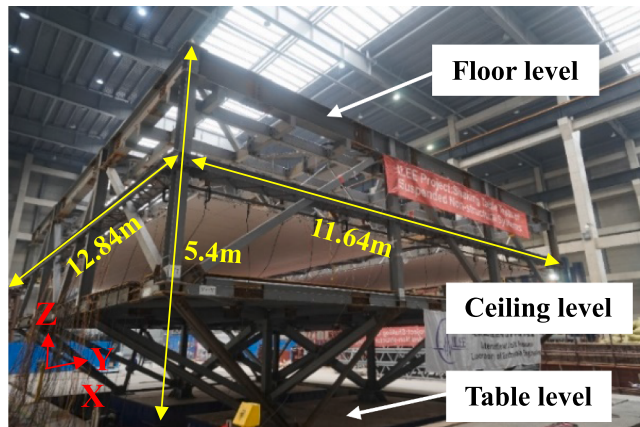


Fig. 4. Schematic view of displacement mechanism on grids with different peripheral connections: (a) SCS without seismic clip connections; (b) SCS with seismic clip connections.



**Fig. 5.** Working mechanism of ceiling grid with semi-free condition: (a) pre-slipping stage, (b) slipping stage, (c) pounding stage.

to hang the SCS. **Fig. 6** shows the overall view of the platform. It has two stories with the height of 5.40 m. The plan dimensions are 12.84 m × 11.64 m. The longitudinal (12.84 m) and transverse sides (11.64 m) of the platform are defined as X and Y directions, respectively. Three levels along the height of the platform, table level, ceiling level, and floor level, are considered. Due to the fact that one shaking table is not big enough to installed the specimen, two shaking tables connected together as an integral one is used in this test.



**Fig. 6.** Overall view of steel platform.

### 3.2. Test specimen

The double-layer SCS with mineral wool boards widely used in public buildings in China is considered here, as shown in **Fig. 7**. One ceiling with the plane area of 150 m<sup>2</sup> is designed, constructed, and suspended from the bottom of the roof of the platform according to Chinese standard J502-2 [17]. The ceiling is comprised of threaded rods, carrying channels, a grid system, lay-in panels, and accessories. Threaded rods hung from the bottom of floor level are the load-carrying members to hang carrying channels, the grid system and lay-in panels. The carrying channel is mainly used to facilitate leveling the ceiling. The grid system consists of main tees, cross tees and sub cross tees, forming a module for placing lay-in panels. Wall angles fixed to the side wall supply vertical support for the grid system. The typical accessories include hangers hung by threaded rods to support carrying channels, hooks connecting carrying channels and main tees, and seismic clips constraining the peripheral grids to the wall angles. It is noted that the configuration of cross-sub cross tee connection is basically identical to that of main-cross tee connection. The detailed information of the ceiling components is presented in **Table 1**.

The boundary condition of the SCS with SFCs on all sides, side 1 to 4, is also shown in **Fig. 6**. Two types of peripheral grids with the same boundary condition, i.e. main tees and sub cross tees, are attached to the wall angles by SFCs on side 1. Only one type of peripheral grids, i.e. cross tees, is connected to the wall angles by SFCs on side 2. The boundary condition of sides 3 and 4 is identical to that of sides 1 and 2, respectively. **Table 2** shows the constraints of 6 degrees of freedom (DOF) at

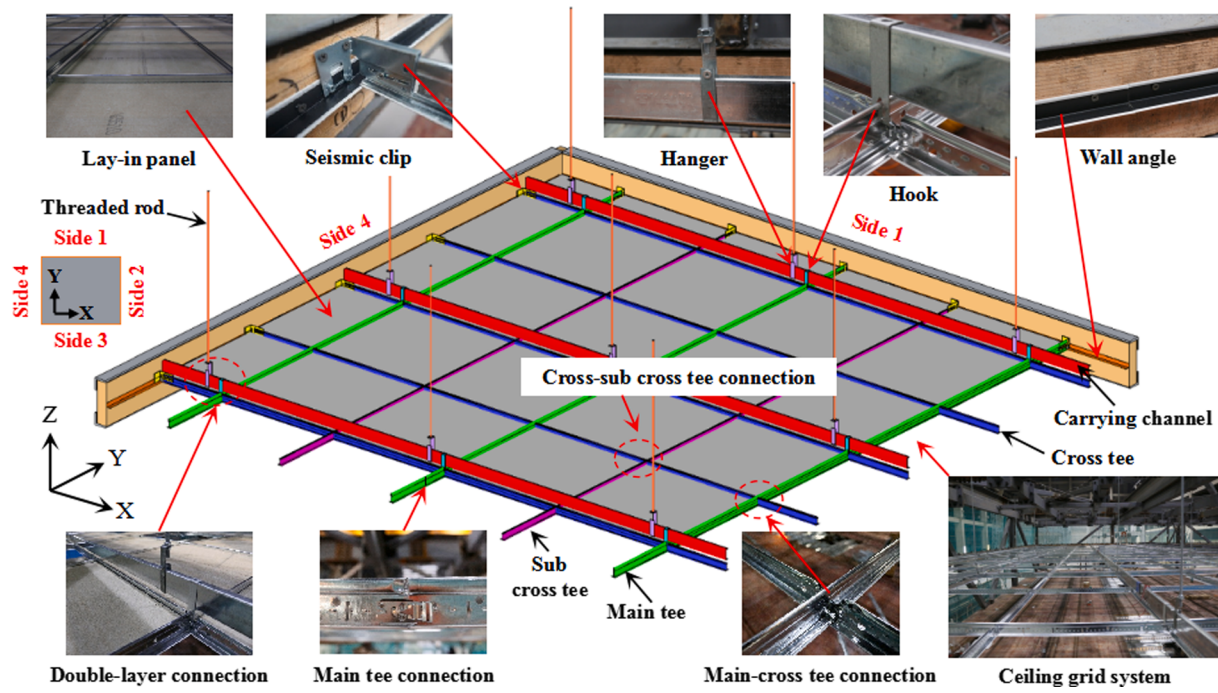


Fig. 7. Composition of the double-layer SCS with mineral wool boards.

**Table 1**

Detailed information of the ceiling components.

Component type	Section (mm)	Length (mm)	Spacing (mm)	Unit mass (kg/m)	Section area (mm <sup>2</sup> )
Threaded rod	M8	1000	1200	0.37	40
Carrying channel	U50 × 15 × 1	4000	1200	2.24	70
Main tee	T43 × 24 × 0.54 × 0.27	3600	1200	1.07	38
Cross tee	T35 × 24 × 0.54 × 0.27	1200	600	0.31	33
Sub cross tee	T30 × 24 × 0.54 × 0.27	600	1200	0.13	28
Wall angle	L22 × 22 × 0.5	3000	N/A	0.53	22
Hanger	–	–	1200	–	–
Hook	–	–	1200	–	–
Seismic clip	–	–	600	–	–
Lay-in panel	600 × 600 × 16	–	/	1.20*	9472

Notes:

1. The section area of ceiling component is obtained by measured data.
2. 1.20\* for lay-in panel refers to the mass of one panel.

**Table 2**

Boundary condition of the ceiling.

Side No.	Constraint of DOF					
	U <sub>X</sub>	U <sub>Y</sub>	U <sub>Z</sub>	R <sub>X</sub>	R <sub>Y</sub>	R <sub>Z</sub>
Side 1	1	0	1	1	1	1
Side 2	0	1	1	1	1	1
Side 3	1	0	1	1	1	1
Side 4	0	1	1	1	1	1

Notes: U<sub>X</sub>, U<sub>Y</sub>, and U<sub>Z</sub> represent the horizontal degrees of freedom along X, Y, and Z axes; R<sub>X</sub>, R<sub>Y</sub>, and R<sub>Z</sub> represent the rotational degrees of freedom along X, Y, and Z axes; and 1 and 0 represent constrained and unconstrained, respectively.

the boundary of the SCS.

### 3.3. Instrumentations

There are 3, 4 and 11 accelerometers installed on table level, ceiling level and floor level of the platform, respectively. The measured acceleration at table level can be regarded as input acceleration of the steel platform. The measured acceleration at floor level can be regarded as input acceleration of the ceiling. A total of 236 instruments including 30 accelerometers (A1-A30), 40 displacement transducers (D1-D40) and 166 strain gauges (S1-S166) are installed on the ceiling to measure the dynamic responses of the ceiling. The location and number of instruments on the ceiling are shown in Fig. 8. The hollow one-way red arrow and blue arrow refer to the positive directions of displacement and acceleration, respectively. The data measured by the accelerometer is the absolute acceleration. The data measured by displacement transducer is the displacement of the ceiling relative to the platform. Except for lay-in panels with strain rosette installed, two strain gauges are attached to both sides of the same position of each ceiling component, and the average of the results obtained from two gauges is used in subsequent data analysis. Only the measurement points for subsequent analysis are marked.

Fig. 9 shows the setup details of displacement transducer on cross tee. It should be noted that the deformation of the main-cross tee connection between the target and the side wall is included in the measured displacement of the cross tee while the measured displacement of main tee does not include such kind of deformation. The measured displacement of the cross tee contains both the relative movement between the ceiling and side wall (equals to the sliding distance within the gap at the ceiling perimeter) and the deformation of main-cross connections. The sliding distance within the gap can be easily determined by the negative displacement measured by the displacement transducer.

### 3.4. Loading protocol

Table 3 lists all the motions input in the test. After each run white noise with the PGA of 0.05 g is input to the specimen to assess the

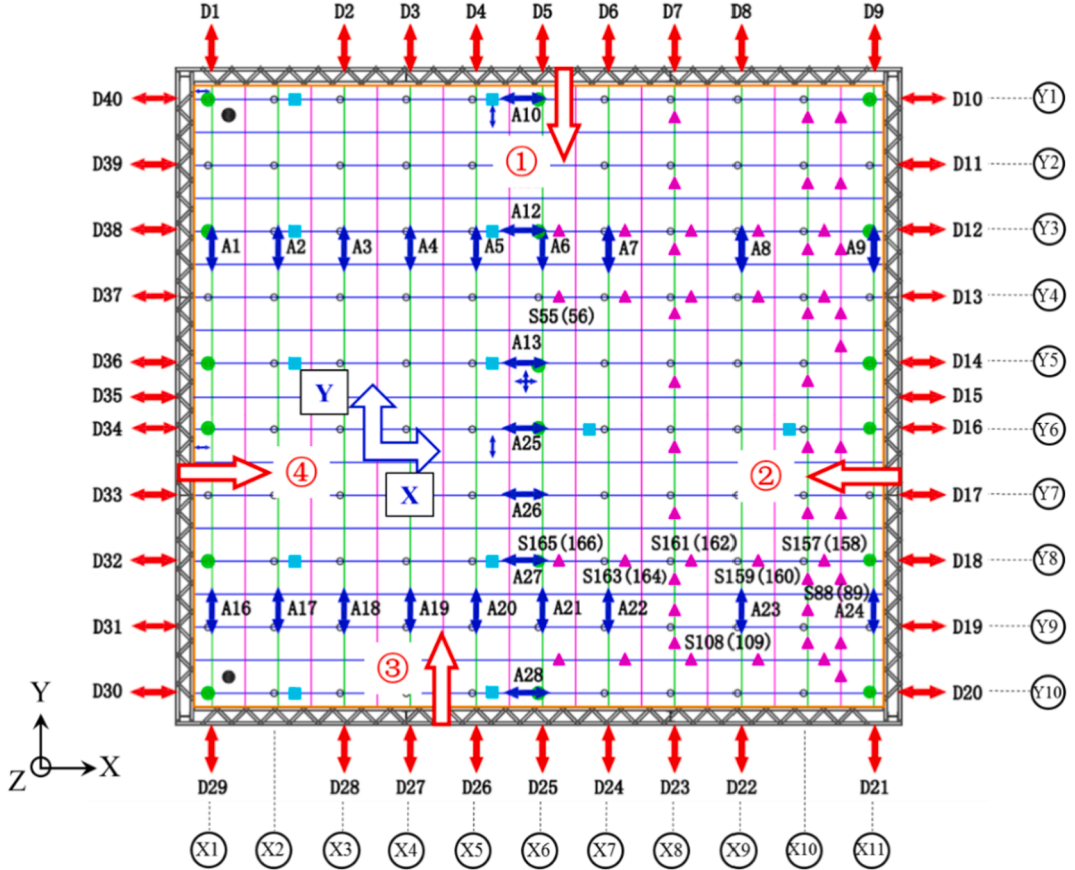


**Fig. 8.** Instrumentations on the ceiling. Notes: → displacement transducer; ← accelerometer; ● strain gauge on threaded rod; ● strain gauge on lay-in panel; ▲ strain gauge on cross tee and sub cross tee; ■ strain gauge on carrying channel.

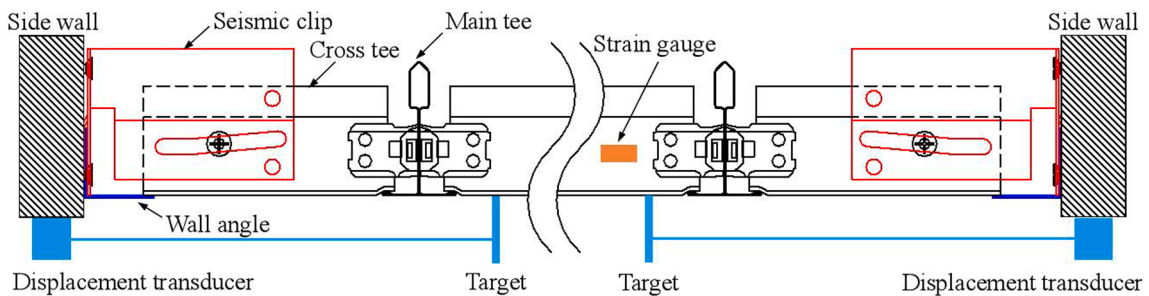


**Fig. 9.** Setup of displacement transducer on cross tee.

dynamic characteristics of the specimen. Several sets of motions are selected and input to the shaking table, including sweep waves (named as Sweep), acceleration responses at different floors of building structures obtained by time history analysis, and artificial wave (named as BCJ-L2). Fig. 10 presents the sweep wave that is the sine wave with the frequency varying from 6.0 Hz to 0.8 Hz. The peak floor acceleration (PFA) at floor level of the platform is listed in Table 3. The input motions, SHW6 (5/128), SHW6 (128/128) and SHW6 (30/30) represent the acceleration responses at the 5th floor and the top of a 128-story supertall structure model and the acceleration responses at the top of a 30-story stick model subjected to the ground motion SHW6 with PGA of 0.1 g, respectively. The floor acceleration responses are closely related to the dynamic properties of the main structure. The natural vibration periods of the first three modes of the 128-story model are

8.94 s, 8.93 s, and 4.48 s, respectively. The corresponding results of the 30-story model are 3.01 s, 1.18 s, and 0.72 s, respectively. The characteristic period of the ground motion SHW6 is 0.9 s. The PFA of SHW6 (128/128) is 1.7 times that of SHW6 (5/128). The fundamental period of the 30-story model is closer to the characteristic period of the ground motion SHW6 than that of the 128-story model, so the PFA of SHW6 (30/30) is larger than that of SHW6 (128/128).

It should be noted that it is extremely difficult to identify the natural frequency of the ceiling by using white noise because the excitation intensity is too low to overcome the initial friction force existing in the ceiling perimeter, causing the ceiling to move with the platform together. Thus, the natural frequency of the ceiling derived by the transfer function method is very close to that of the platform [18,19]. Further information about the input motions is provided in Reference

**Table 3**  
Details of motions input to specimen.

Run No. <sup>1)</sup>	Name of input motion	Target acc. of table (g)		Duration (s)	PFA of platform (g)	
		X dir.	Y dir.		X dir.	Y dir.
2	Sweep	0.050	0	100	0.071	–
4	Sweep	0	0.050	100	–	0.087
6	Sweep	0.050	0.050	100	0.069	0.087
8	BCJ-L2	0.037	0	120	0.050	–
10	BCJ-L2	0	0.037	120	–	0.057
12 <sup>2)</sup>	SHW6 (5/128)	0.089	0.070	70	0.127	0.098
14 <sup>2)</sup>	SHW6 (128/128)	0.149	0.132	70	0.146	0.153
16 <sup>2)</sup>	SHW6 (30/30)	0.405	0.377	150	0.571	0.573
18	Sweep	0.150	0	100	0.225	–
20	Sweep	0	0.150	100	–	0.242
22	Sweep	0.150	0.150	100	0.232	0.277
24	Sweep	0.250	0	100	0.393	–
26	Sweep	0	0.250	100	–	0.512
28	Sweep	0.350	0	100	0.572	–
30	Sweep	0	0.350	100	–	1.942
32	Sweep	0.500	0	100	1.319	–

Notes:

<sup>1)</sup> Runs of odd number used for white-noise excitation with small magnitude are not listed in the table.

<sup>2)</sup> During Runs 12 and 14 the floor acceleration responses at the 5th and 128th floors of the 128-story building subjected to the ground motion SHW6 are input, and during Run 16 the floor acceleration response at the 30th floor of the 30-story building is input.

[19,20].

#### 4. Experimental results and discussions

##### 4.1. Failure pattern and damage evolution

The typical damage to the ceiling components observed in the test is shown in Fig. 11. The failure of hanger and hook is a special damage mode in the double-layer SCS due to its different construction details from other types of SCSs. It can be found that most damage is associated with grid connections, which indicates that the most vulnerable part of the ceiling is the grid connection. No damage to SFCs is observed during the loading process. Compared to the free boundary condition without any attachments, such as seismic clips, the semi-free boundary condition plays the role in preventing the unseating of the peripheral grids from the wall angles. The semi-free boundary condition achieved by seismic clips with four perimeter screws can avoid experiencing excessive twisting and deformation of seismic clip connection due to insufficient perimeter screws. Thus, it is suggested that all available perimeter screws at the flange of seismic clips should be fixed to the perimeter to improve the strength of the peripheral connections of the SCS.

The damage process of the ceiling is demonstrated in Fig. 12. No damage to the ceiling is observed before Run 16. The pulling out of a main-cross tee connection and buckling of the grid connections near the perimeter are found under Run 16. The main-cross tee connection fails mainly due to the reason that the axial force acting on it is greater than its strength. The grid connections near the perimeter are vulnerable to

buckling since the cumulative axial force acting on the grid connections near the perimeter reaches the maximum during the collision. With an increase in the PFA, the damage to the ceiling gradually becomes obvious but is still slight after Run 26. When the PFA reaches 1.942 g in the Y direction during Run 30, the buckling and pulling out of a large number of grid connections and the dislodgement and falling of some panels around the ceiling perimeter occur. It should be noted that the failure of main tee connections during Run 30 greatly accelerates the collapse of the ceiling. After the input of sweep wave with the highest PGA of 0.5 g in X direction, the ceiling completely collapses with the ratio of falling panels to total panels reaching 40.68%.

The authors investigated the seismic performance of double-layered SCSs with three types of boundary condition by shaking table tests, i.e. free boundary condition (BC1), fixed-semi-free boundary condition (BC2), and semi-free boundary condition (BC3). The detailed comparison of the experimental results of SCSs with free boundary condition (BC1) and fixed-semi-free boundary condition (BC2) can refer to the Reference [19]. Fig. 13 shows the comparison of variation of the proportion of damaged grid connections (PDGCs) of SCSs with different type of boundary condition with increased PFA. When the PFA is smaller than 0.5 g, the PDGC of SCSs with different type of boundary condition is almost the same. As the PFA increases beyond 0.5 g, the PDGC of SCS with free boundary condition (BC1) is the highest due to the failure of a large number of peripheral connections caused by weak boundary constraint, and the PDGC of SCS with fixed-semi-free boundary condition (BC2) is the lowest. In general the SCS with fixed-semi-free boundary condition (BC2) exhibits superior seismic performance compared to that with semi-free boundary condition (BC3).

In this study the BC3 is proposed mainly for the following two reasons: (1) the fixed edges of SCSs with fixed or fixed-semi-free boundary condition may be damaged under earthquakes because the strong boundary constraint on the fixed edges allows inertia forces induced in SCS to transfer and accumulate at the peripheral fixings. Therefore, all fixed edges are adjusted to semi-free edges to explore the seismic performance of SCS with BC3. (2) in the current practice the construction measures for semi-free seismic clip connections at the boundary are inadequate, i.e., the flange of seismic clip is not firmly connected to the surroundings due to the lack of sufficient perimeter screws, which often leads to damage to these connections. Therefore, in this study all seismic clips of SCS with semi-free boundary condition are attached tightly to the surroundings by using all available perimeter screws to improve the seismic capacity of semi-free seismic clip connections.

In the case of large-area SCS, when the accumulated axial force demand on the fixed connection of the SCS with BC2 is larger than its capacity, the fixed connection may be damaged. For the SCS with BC3, the release of boundary constraints caused by the semi-free boundary condition can reduce the axial force demand on the connection at the perimeter to prevent the damage. In addition, if the gap between the grid end and wall angle is set reasonably, the adverse effect of the collision on the seismic performance of the SCS with BC2 can be reduced or avoided.

##### 4.2. Acceleration time history of ceiling grid

An example of the acceleration time history of channel A13 located in the middle of axis Y5 in X direction in the case of 0.15 g sweep in X

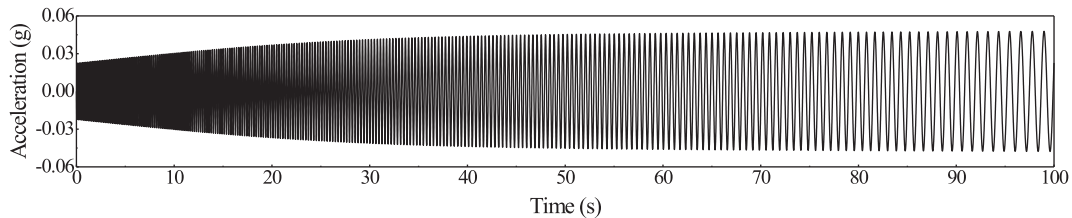
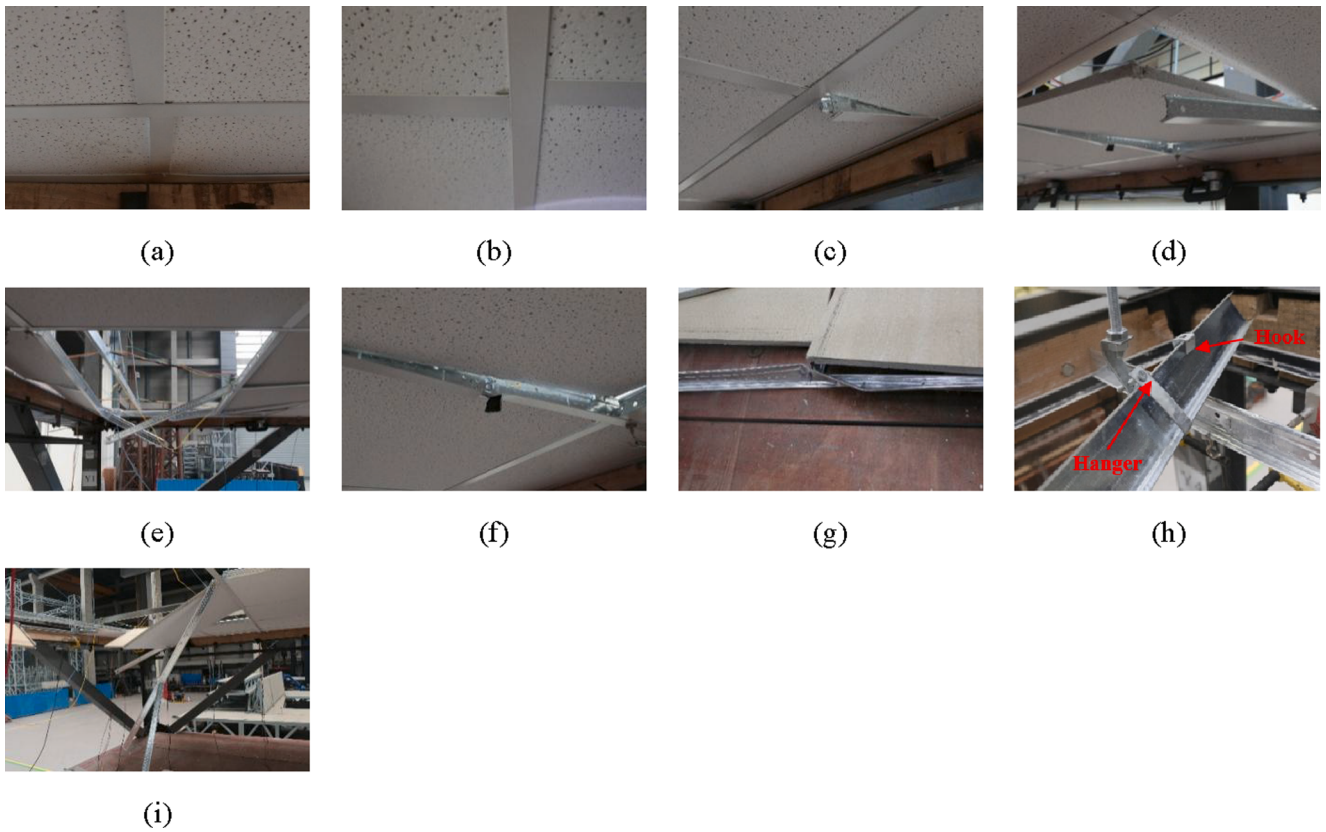


Fig. 10. Sweep wave.



**Fig. 11.** Typical damage to ceiling components: (a) buckling of main-cross tee connection, (b) buckling of cross-sub cross tee connection, (c) separation of main-cross tee connection, (d) dislodged panel, (e) falling of panel, (f) separation of main tee connection, (g) buckling of grid, (h) failure of hanger and hook, (i) falling of grid.

direction is shown in Fig. 14 (see the location of A13 in Fig. 8). The acceleration of the grid gradually increases during the slipping stage. There is a significant amplification of acceleration being 10 times the PGA of input during the pounding stage because the relative displacement of the ceiling exceeds the gap, resulting in the violent impact between the grid end and the boundary. A lot of high spikes appear in the acceleration time history. The pounding starts at around 50 s with the input frequency of 2.3 Hz. Then the acceleration increases significantly. Unlike the violent impact from the beginning of loading in Ceiling A with smaller width of gap [19], the gap with larger width in the ceiling here delays the impact. The SFCs prevent the peripheral grids from falling down so that it leads to the continuous impact regardless of the intensity of the input.

#### 4.3. Displacement time history of ceiling grid

Fig. 15 shows the results of channels D33 and D17 located at the left and right ends of axis Y7 in X direction in the case of 0.15 g sweep in X direction (see the location of D33 and D17 in Fig. 8). The deformation is defined as the deformation of the grid system between two displacement transducers, as shown in Fig. 15c. From Fig. 15a it can be found that the pounding occurs at around 50 s when the input frequency is 2.3 Hz. Due to the semi-free boundary condition, the ceiling in this test exhibits stable slipping and pounding behavior. The displacement gradually increases during the slipping stage, and it reaches the width of the gap at the boundary during the pounding stage with the residual displacement of 5 mm. Notable residual displacement is caused by the friction force between the middle slot and sliding screw of seismic clip and the damage to the ceiling. Due to the effect of SFCs at the ends of the row of grid, the displacement amplitudes of two transducers are roughly equal, and the displacement directions are opposite, which is consistent with the movement characteristic of the grid (Fig. 15b). It can be concluded that

the semi-free boundary condition could change the movement behavior of the SCS.

The SFC could adapt to the large movement of the ceiling so that the displacement response of the ceiling is stable. Fig. 16 shows the movement process of grid in cross tee direction (X direction) in the case of 0.15 g sweep. The cross tee line consists of 12 pieces of cross tees and 11 connections. The original distance between the displacement transducers is  $L_0$ . The displacement measured by transducers equals to the sum of the displacement of slipping on the wall angle and deformation of the end connection. The maximum positive and negative displacements of D33 are 14 mm and -15 mm, respectively. Those of D17 are 16 mm and -13 mm, respectively. When the grid moves to the right side, the deformation and average displacement of the grid system are 1 mm and 13.5 mm, respectively. When the grid moves to the left side, the deformation and average displacement of the grid system are 1 mm and 15.5 mm, respectively. The connection at the left end buckles due to the pounding during the movement of the grid. Although the connection buckles, the deformation of the components between the two transducers is not affected by the buckling behavior since the buckling does not occur in the components between the two transducers. Compared with the deformation of the grid system, the average displacement is much bigger. The most important difference between main tee direction and cross tee direction in the grid is the number of connections. The main tee line consists of 4 pieces of main tees and 3 connections. The displacement measured by the transducer in main tee direction does not include the deformation of connections since there are no main tee connections existing between the transducer and the perimeter.

#### 4.4. Acceleration versus displacement relationship

Fig. 17 shows the acceleration versus displacement relationship of the typical position in the ceiling. Run 18 and Run 20 are selected as the

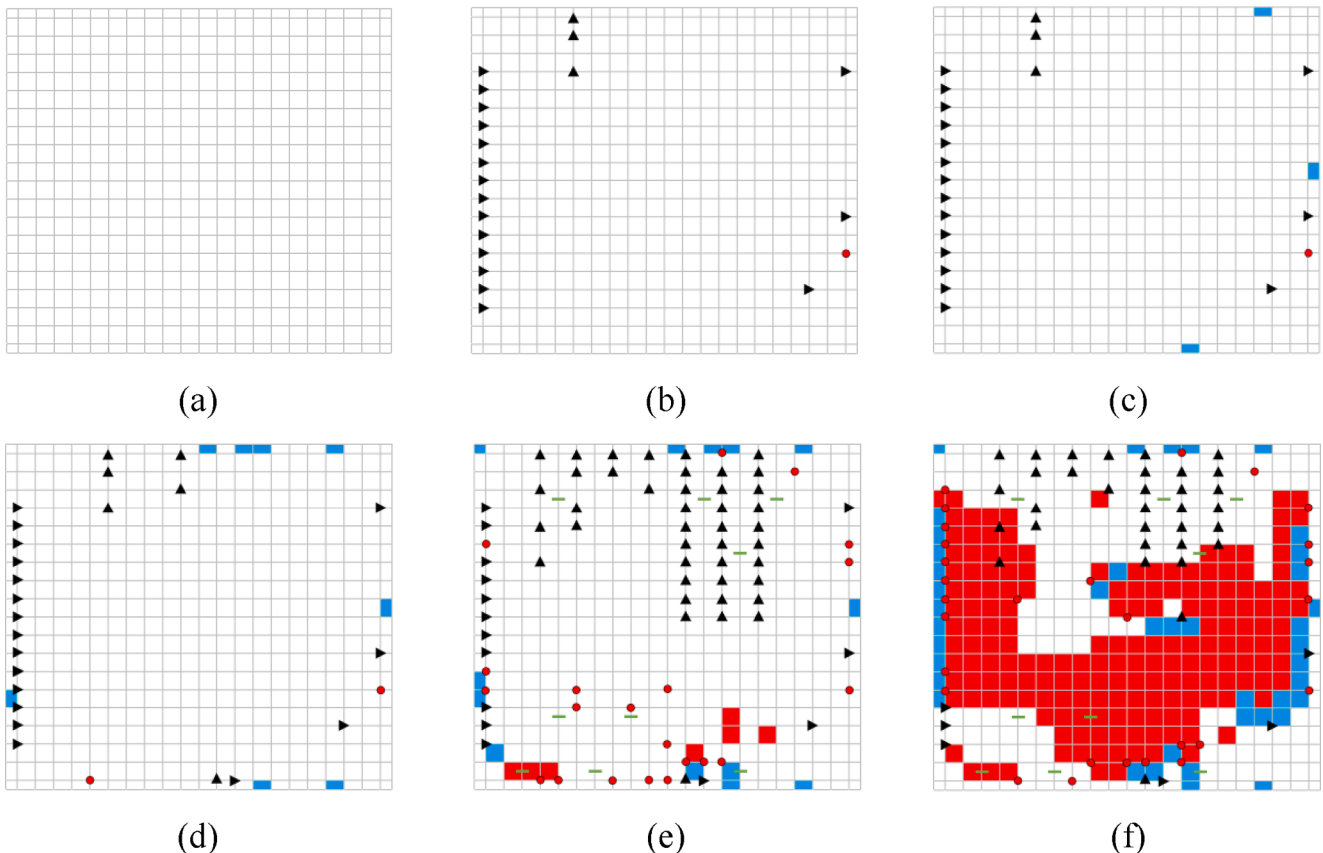


**Fig. 12.** Damage process of the ceiling: (a) Before Run 16, (b) 0.405 g (X) & 0.377 g (Y) Random (Run 16), (c) 0.15 g (X) & 0.15 g (Y) Sweep (Run 22), (d) 0.25 g (Y) Sweep (Run 26), (e) 0.35 g (Y) Sweep (Run 30), (f) 0.5 g (X) Sweep (Run 32). Notes: ▲ buckling of main-cross tee connection; ▲ buckling of cross-sub cross tee connection; ● separation of main-cross tee connection and cross-sub cross tee connection; ■ dislodgement of panel; ■ falling of panel; — separation of main tee connection.

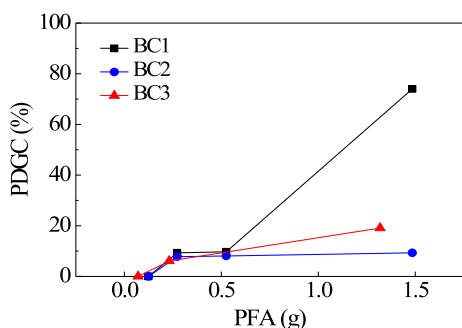


**Fig. 13.** Comparison of variation of proportion of damaged grid connections of suspended ceilings with different type of boundary condition with increased PFA.

representatives of pounding stage in X direction and Y direction, respectively. During Run 18, the measuring points A27 and D18 located in the axis Y8 are selected. During Run 20, the measuring points A6 and D5 located in the axis X6 are selected. It can be found from Fig. 17a that during the pounding stage, the acceleration changes drastically during pounding, and the acceleration reduces quickly to around zero after pounding. Due to the existence of SFCs, the curve reflects both friction-slip and pounding behavior. The slipping stage increases the energy dissipation by the friction mechanism between middle slot and sliding screw along the axial direction of the perimeter grid.

Compared with the responses in X direction, in Y direction the acceleration reaches the peak more quickly and the peak acceleration is larger, which is related to the arrangement of different components in

two directions and different details between main tee connections and main-cross tee connections. There are fewer connections for main tees in a line in Y direction, and the capacity of resisting buckling of the main tee connections is larger due to the construction details, causing smaller deformation of the main tee connections and greater acceleration of the main tees.

#### 4.5. Acceleration amplification factor

In the current seismic design codes in most countries, the equivalent static method is recommended for calculating the seismic action of non-structural components, in which the component acceleration amplification factor (AAF) is a key parameter. The AAF is calculated as the ratio of the peak ceiling grid acceleration (PCGA) to the peak floor acceleration (PFA). The peak AAF prescribed in Chinese seismic design code takes the value of 2.0 for the suspended ceiling system [21].

The AAF of the ceiling under sweep waves is shown in Fig. 18. Under Runs 2, 4 and 6, the AAF of the ceiling is around 1.5. In these cases, the ceiling is in the pre-slipping stage and no pounding occurs in the ceiling. The AAF increases with the increase of input intensity due to significant pounding before Run 28. The AAF reduces significantly during Run 30 with larger PFA due to more severe damage to main tee connections. The AAF at most measuring points is roughly uniform except the endpoints. The AAF at both ends in X direction is the smallest due to the greater constraint from SFCs in Y direction. Similarly, the AAF at both ends in Y direction is much less than that between the two ends in Y direction. The largest AAFs in X and Y direction are 9.7 and 9.4, respectively, which is caused by the huge pounding at the boundary. It is necessary to develop seismic measures to reduce pounding. Adding the isolation foam in the

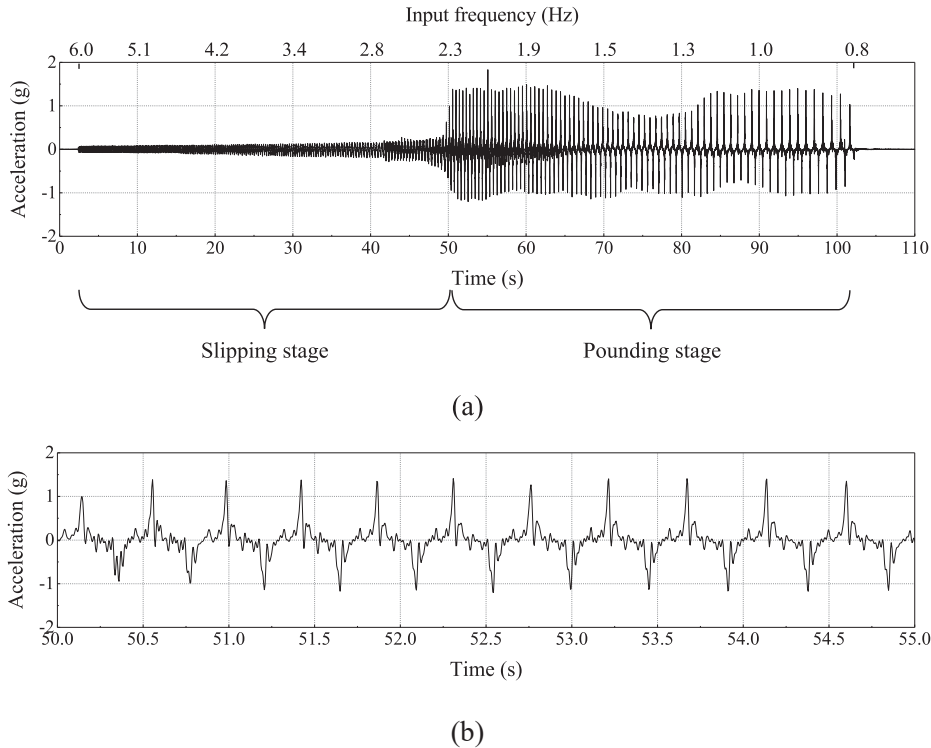


**Fig. 14.** Acceleration time history of channel A13 under 0.15 g sweep in X direction (Run 18): (a) total acceleration time history, (b) acceleration time history during pounding.

peripheral gap may be possible. The median AAF under sweep waves is 3.3, which is larger than the median AAFs of 3.2 and 2.9 reported in UB and UNR, respectively [8]. It is mainly due to the violent impact caused by the semi-free boundary condition in the ceiling.

The AAF of the ceiling under excitations of artificial wave and floor earthquake waves is plotted in Fig. 19. Whether in X direction or Y direction, the AAF increases as the input intensity increases. From Run 8 to 12, the AAFs of the ceiling are around 1.0, indicating that the ceiling is in the pre-slipping stage. During Run 14 without pounding behavior, most of AAFs in X direction are greater than those in Y direction due to the smaller lateral stiffness in X direction. Among the acceleration responses of all Runs, the AAF in Run 16 is the highest due to the pounding. During Run 16, the AAFs in X direction are smaller than those in Y direction due to the fact that more serious damage to main-cross tee connections in X direction reduces the acceleration response of the ceiling in X direction. The median AAF under the excitations of floor earthquake waves is 1.2, which is lower than 2.0 which is suggested by the design code [21].

For the three types of floor earthquake waves, the AAF is the largest in Run 16 (SHW6 (30/30)), the second largest in Run 14 (SHW6 (128/128)), and the smallest in Run 12 (SHW6 (5/128)), indicating that the type of input seismic wave has significant effect on AAF. It is found that both of the type and intensity of input seismic wave have significant effect on AAF. In this study only a small number of seismic waves were input. Therefore, the authors think that a large amount of seismic waves should be input in further study to obtain reliable AAF for seismic design of suspended ceilings.

#### 4.6. Peak displacement

The peak displacement (PD) under unidirectional sweep excitations is shown in Fig. 20. From Run 2 to 6, the PD is close to zero, which implies that the ceiling moves with the platform together. The PD of the ceiling is more uniform at the middle and smaller on both sides as the result of the constraint effect of SFCs in the perpendicular direction. In X direction, the PD of the middle points reaches the width of the gap

between the grid end and wall angle during Run 18. The PD during Run 22 is almost the same as that during Run 18. Due to the buckling of the grid connections and more serious damage to the grid ends after Run 22, the width of the gap becomes larger, which causes the increase of PD. In Y direction, the PD of the middle points reaches the width of the gap during Run 20, which is close to the PD during Run 22. Most of PDs during Run 26 are greater than the width of the initial gap, which indicates that the gap increases due to the local buckling of the grid ends and deformation of the grid. Whether in X or Y direction, the PD increases with the increase of intensity of sweep wave.

Fig. 21 presents the PD of measuring points under artificial wave and floor earthquake waves. From Run 8 to 12, the PD of the ceiling is small. During Run 14, the PD is smaller than the width of the gap, indicating that no pounding occurs at the boundary. During Run 16, the PD firstly exceeds the width of the gap, indicating that the pounding begins at the boundary. The PDs of the ceiling are roughly uniform at the middle and smaller on both sides. The floor earthquake wave with higher intensity produces larger PD. For the three types of floor earthquake waves, the AAF is the largest in Run 16, the second largest in Run 14, and the smallest in Run 12. Compared with the measured PDs in the ceiling without seismic clips [19], the PDs in the test are larger under the seismic excitation with same intensity, which is mainly caused by the larger width of the peripheral gap.

#### 4.7. Strain of ceiling component

The recorded maximum strains of the ceiling components before the ceiling collapses (Run 32) are listed in Table 4. The yield strain of ceiling components is  $1175 \mu\epsilon$ . All components remain elastic. However, the local buckling is observed in some grids due to strong pounding between the ceiling and the boundary. The strain of the threaded rod is much larger than that of other components. The maximum strain is  $598 \mu\epsilon$  and  $526 \mu\epsilon$  under sweep waves and floor earthquake waves before the ceiling collapses, respectively, which is much larger than the maximum strain recorded in the test with smaller peripheral gap [19]. It is because the

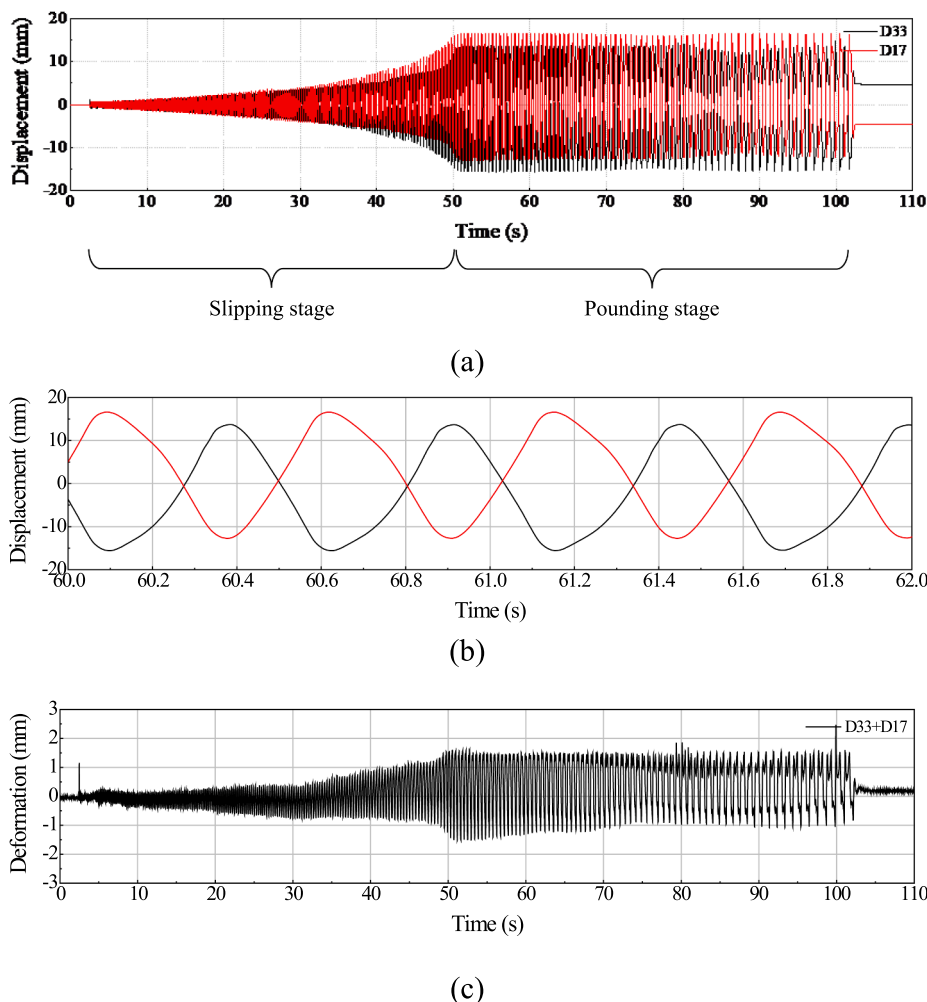


**Fig. 15.** Results of a pair of displacement transducers under 0.15 g sweep in X direction (Run 18): (a) displacement time history of a pair of transducers, (b) displacement time history from 60 s to 62 s, (c) deformation of the ceiling.

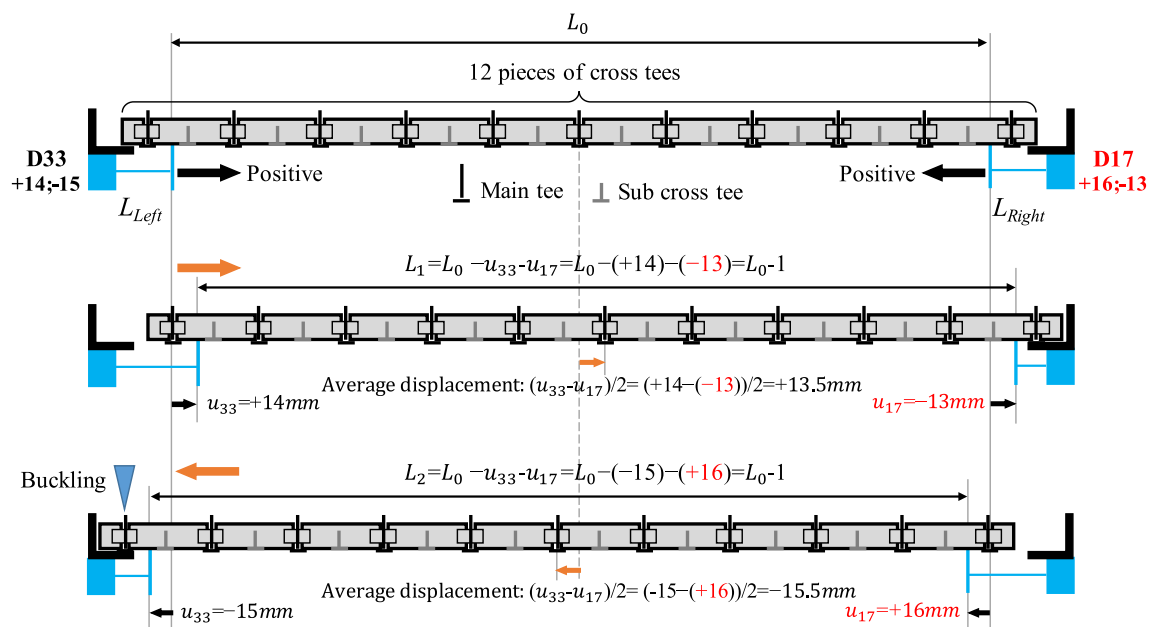


**Fig. 16.** Movement process of grid in cross tee direction under 0.15 g sweep in X direction (Run 18).

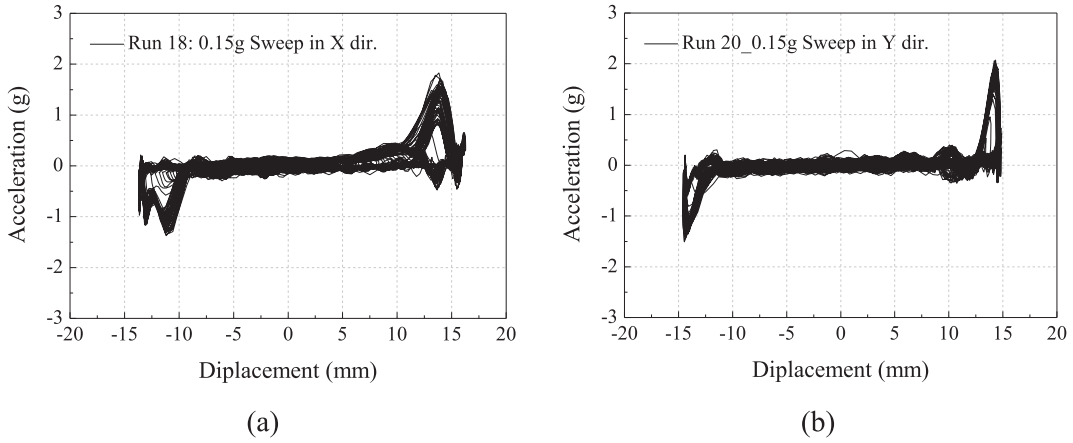


**Fig. 17.** Acceleration versus displacement relationship: (a) pounding stage in X direction, (b) pounding stage in Y direction.

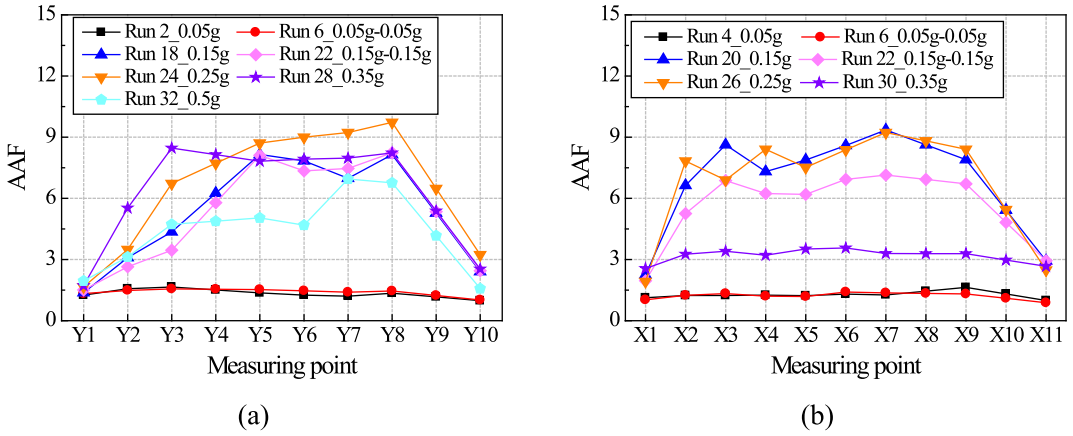


**Fig. 18.** Acceleration amplification factor under sweep waves: (a) response in X direction, (b) response in Y direction.

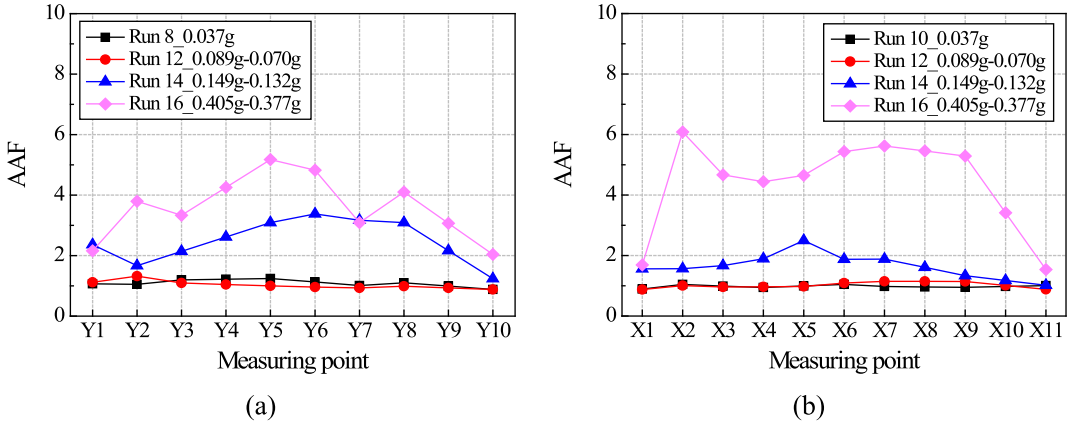
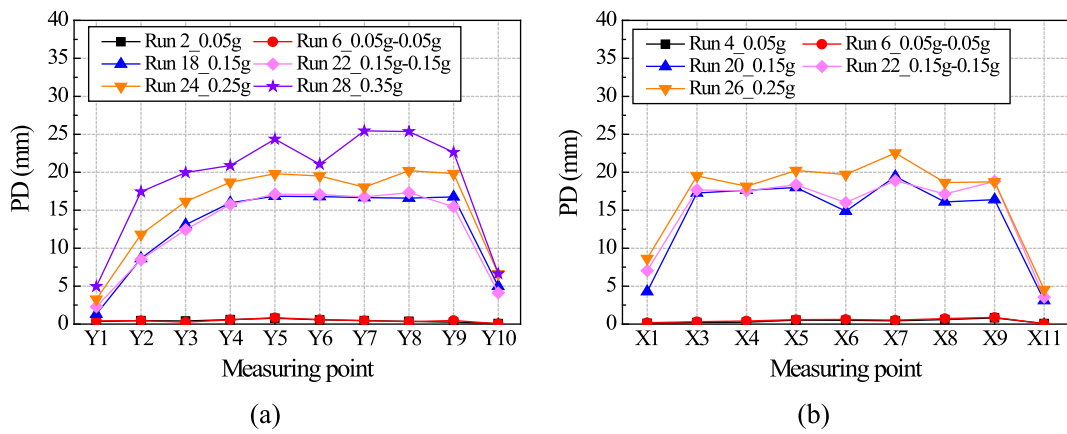


**Fig. 19.** Acceleration amplification factor under artificial wave and floor earthquake waves: (a) response in X direction, (b) response in Y direction.

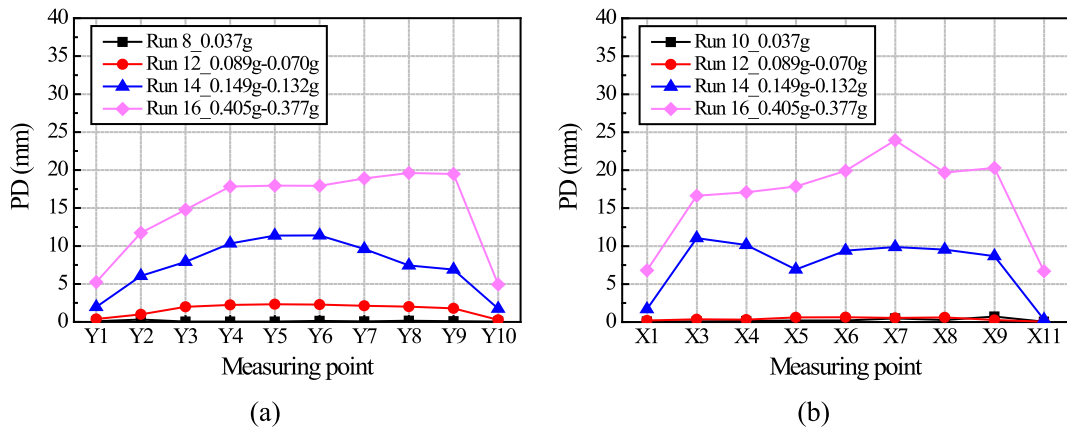
larger peripheral gap at the ceiling perimeter in the test increases the relative deformation of the threaded rod, further resulting in greater strain in the threaded rod.

Fig. 22a and 22b present the peak strain versus PCGA relationship of the representative positions in ceiling grids under sweep waves and floor earthquake waves, respectively. The measuring point (S108/S109) on the main tee is located at the end of axis X8 (see the location of the strain gauges in Fig. 8). The measuring point (S55/S56) on the cross tee is located at the middle of axis Y4. The measuring point (S88/S89) on the sub cross tee is near the end between axis X10 and axis X11. Under

sweep waves four levels of PCGA corresponding to inputs with PGA of 0.05 g, 0.15 g, 0.25 g and 0.35 g are considered. Under floor earthquake waves four levels of PCGA corresponding to inputs with PGA of 0.037 g, 0.089 g, 0.149 g and 0.405 g are considered. For the main tee, the peak strain continues to increase as the input intensity increases. No buckling occurs in the main tee connections. The strain of main tee is significantly affected by pounding which induces the axial force. For the cross tee and the sub cross tee, the peak strain response increases linearly with the increase of input intensity. The maximum peak strain is smaller than that of main tee, due to the buckling of connections.



**Fig. 20.** Peak displacement under sweep waves: (a) response in X direction, (b) response in Y direction.



**Fig. 21.** Peak displacement under artificial wave and floor earthquake waves: (a) response in X direction, (b) response in Y direction.

**Table 4**

The maximum strain of ceiling components.

Excitation type	Maximum strain of ceiling component ( $\mu\epsilon$ )				
	Threaded rod	Main tee	Cross tee	Sub cross tee	Carrying channel
Sweep wave	598	67	128	210	130
Floor earthquake wave	526	64	172	78	85

It can be found from Fig. 22b that the strain increases as the input intensity increases. Under the input of the first two levels, the strain is very small due to the fact that the ceiling is in the pre-slipping stage. Under the input of the third level, the ceiling is in the slipping stage, and the strain increases slowly. Under the input of the fourth level, the ceiling pounds on the surroundings, and the PCGA and peak strain increase sharply.

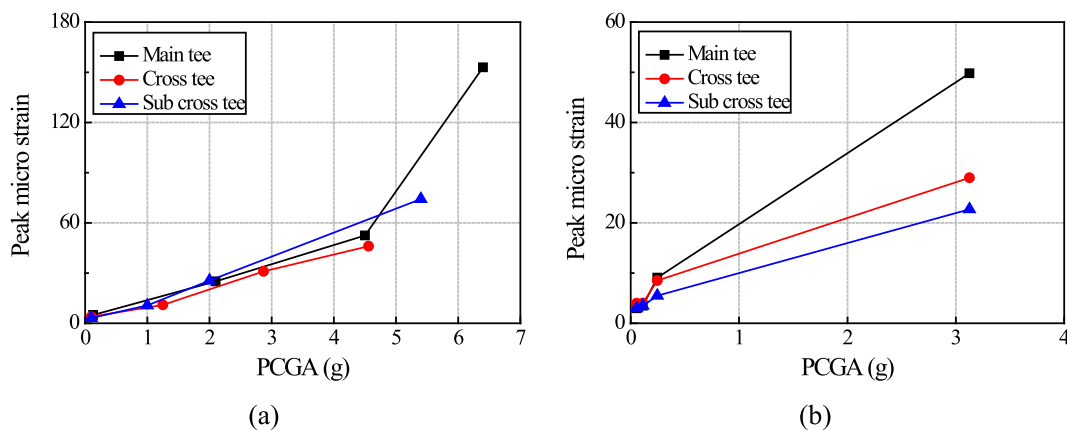


**Fig. 22.** Peak strain versus PCGA relationship: (a) under sweep waves, (b) under floor earthquake waves.

## 5. Numerical simulation

### 5.1. Numerical modeling

Considering the roughly uniform seismic responses of SCS with semi-free boundary condition in the same direction but at different location under the earthquake, the simplified planar numerical model is built by using the software OpenSEES. Fig. 23 presents the analytical model of the tested SCS in X direction as an example. The horizontal acceleration time history at the top of the steel platform is used as the input motions to the analytical model.

The threaded rod is simulated by dispBeamColumn element, and the top of threaded rod is set as fixed. The grid member is simulated by elasticBeamColumn element. The panel is simplified as a lumped mass placed at the grid connection. The ZeroLength element with Pinching4 material is adopted to model the axial nonlinear behavior of grid connection, and the parameters of Pinching4 material are calibrated by the data from the ceiling components conducted by the authors [22]. The double-layer connection is assumed to be pin-connected.

The friction and pounding behaviors at the ceiling perimeter are simulated using the friction model and impact model, respectively. The friction model is modeled using Steel01 material, mainly expressed by three parameters, i.e. initial elastic tangent  $K$ , yield strength  $F_y$ , and strain-hardening ratio  $b$ . Herein, the initial elastic tangent is defined as the ratio between yielding strength and initial displacement of 0.1 mm, and strain-hardening ratio is set very small according to the reference [23]. The yield strength representing the friction force is calibrated by the corresponding shaking table test results and taken as 2 N. According to the friction force and initial displacement, the initial elastic tangent is taken as 20 N/mm. A value of 0.05 for strain-hardening ratio is found to be the best when calibrating the analytical model by comparing the simulation results with the experimental data.

The impact model is modeled using ImpactMaterial material, mainly expressed by four parameters, i.e. initial stiffness  $K_1$ , secondary stiffness  $K_2$ , yield displacement  $\delta_y$ , and initial gap width. The initial stiffness and secondary stiffness are taken as 300 N/mm and 100 N/mm, respectively, to fit the experimental data best. The yield displacement is taken as 0.1 mm. The initial gap width is determined as 13.3 mm by the measured displacement history of grid ends during the shaking table tests.

### 5.2. Comparison of simulation and experimental results

Fig. 24 compare the simulated acceleration time history and experimental results of the tested SCS with semi-free boundary condition. The comparison of the simulated displacement time history and experimental results is shown in Fig. 25. The mean absolute errors of peak

acceleration (the absolute difference between the simulated and test result divided by the test result) within the overall time history for 4 Runs in Fig. 24 are 43.16%, 6.01%, 9.95%, and 21.99%, respectively. This may be due to the errors caused by model simplification and inaccurate parameters of friction and impact models. The mean absolute errors of peak displacement within the overall time history for 4 Runs in Fig. 25 are 12.73%, 10.07%, 10.84%, and 17.67%, respectively. Generally, the calculated acceleration and displacement responses by the proposed simplified analytical model agree well with the test results. A more precise three-dimensional numerical model employing accurate parameters in friction and impact models needs to be studied in the future work. Notably, there are some differences between simulation and experimental results in the high-frequency components of acceleration.

## 6. Seismic design recommendations

During the shaking table test no damage to seismic clip connections was observed. The connections with seismic clips not only prevented the falling of the peripheral grids from the wall angles, but also avoided excessive deformation of seismic clips by using sufficient perimeter screws. Considering that in practice the SCS is usually placed on the peripheral support without any attachments connected with the surroundings in China, it is suggested that the installation of seismic clips for connecting the ceiling grids to the surroundings is necessary. The effectiveness of this method was also proved in the authors' previous work [19,20].

Among all the failure patterns found in the test, most damage was associated with the grid connections, and thus the grid connections were regarded as one of the most vulnerable parts in the SCS and dominant to the earthquake resisting capacity of SCS. The failure of the grid connections may cause the falling of the surrounding panels, and further accelerate the collapse of the SCS during earthquakes. Therefore, strengthening grid connections is the key to improve the seismic performance of the SCS. The cross-shaped seismic clip for strengthening the grid connections was verified to be effective by Pourali [24].

When the SCS with semi-free boundary condition was subjected to strong motions, the displacement of the SCS relative to the surroundings exceeded the width of the gap between the grid end and the wall angle, resulting in severe pounding occurring at the perimeter of the SCS. The pounding harmfully affected the seismic performance of the SCS. Effective seismic measures should be taken to reduce the impact between the SCS and surroundings. On the one hand, the width of the wall angles can be increased to allow larger peripheral gap so as to avoid or reduce the collision at the ceiling perimeter. On the other hand, filling of a compressible material in the peripheral gap may be a good way to

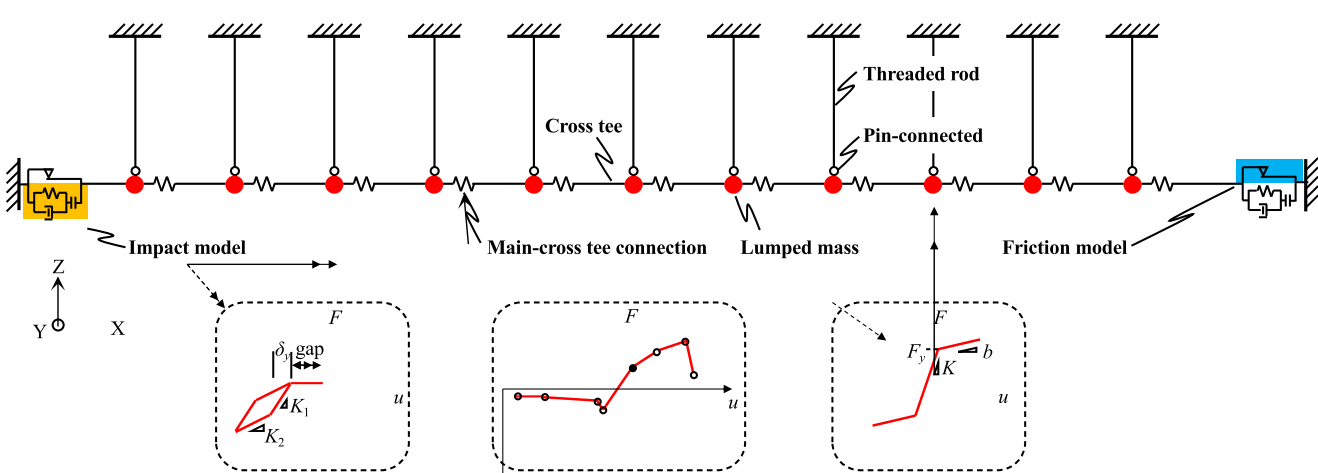
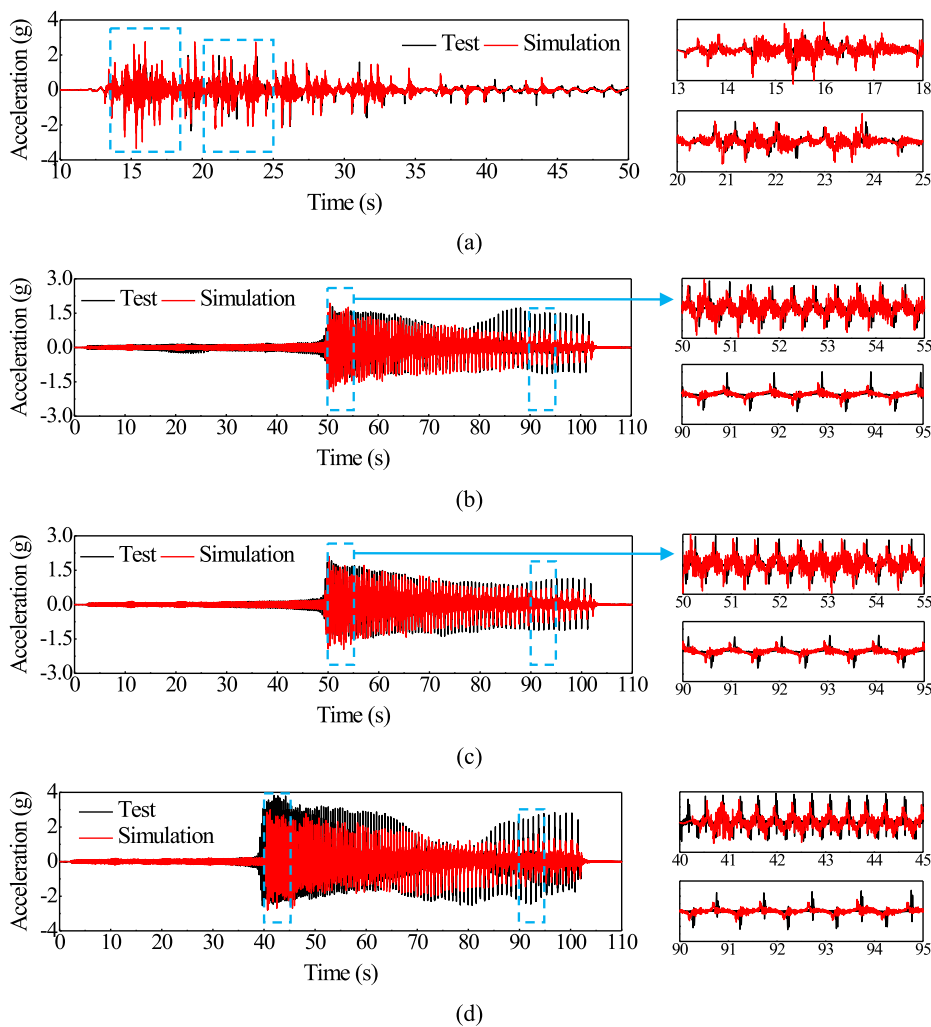


Fig. 23. Simplified analytical model of SCS with semi-free boundary condition.



**Fig. 24.** Comparison of acceleration time history between simulation and experimental results: (a) 0.405 g (X) & 0.377 g (Y) Random (Run 16), (b) 0.15 g (X) Sweep (Run 18), (c) 0.15 g (X) & 0.15 g (Y) Sweep (Run 22), and (d) 0.25 g (X) Sweep (Run 24).

protect the SCS from the pounding effect [25]. These seismic measures need to be further validated through experiments.

## 7. Conclusions

This paper presents a new semi-free boundary condition for the double-layer SCS widely used in China. The full-scale shaking table tests are conducted on the SCS to verify the working mechanism of the SCS with the new boundary condition and investigate the its dynamic behavior. Additionally, a simplified analytical model for the SCS with semi-free boundary condition is proposed. Based on the research results, the following conclusions can be drawn:

- (1) The movement process of the ceiling grid can be divided into three stages: pre-slipping, slipping, and pounding. The responses of SCS during the individual stage reflect different characteristics. During the pounding stage the dynamic responses of SCS are most significant and most of damage to SCS occurs.
- (2) The failure of hanger and hook is a special damage pattern in the SCS. In SCS the grid connections are most vulnerable to the earthquake and dominant to the earthquake resistance capacity of SCS. No damage to the peripheral connections is observed, which is attributed to sufficient perimeter screws connecting the seismic clips and the surroundings. The semi-free boundary condition plays an important role in preventing the unseating of

the peripheral grids from the wall angles and protecting the peripheral connections from damage.

- (3) The median AAF under excitations of floor earthquake waves is lower than the value suggested by Shanghai seismic design code. The displacement of the ceiling relative to the platform reaches the peak at the state that the collision between the ceiling and the boundary occurs. All components remain elastic before the ceiling collapses under the excitations. However, the local buckling of some grids is observed due to strong pounding in the last few runs.
- (4) The impact at the ceiling perimeter harmfully affects the seismic performance of the SCS. Some measures should be taken to reduce the impact.
- (5) The calculated acceleration and displacement responses by the proposed simplified numerical model agree well with the test results.
- (6) In order to mitigate seismic damage to the SCS, some pointed seismic design recommendations are proposed to improve the seismic performance of the SCS.

## Declaration of Competing Interest

The authors declare that they have no known competing financial interests or personal relationships that could have appeared to influence the work reported in this paper.

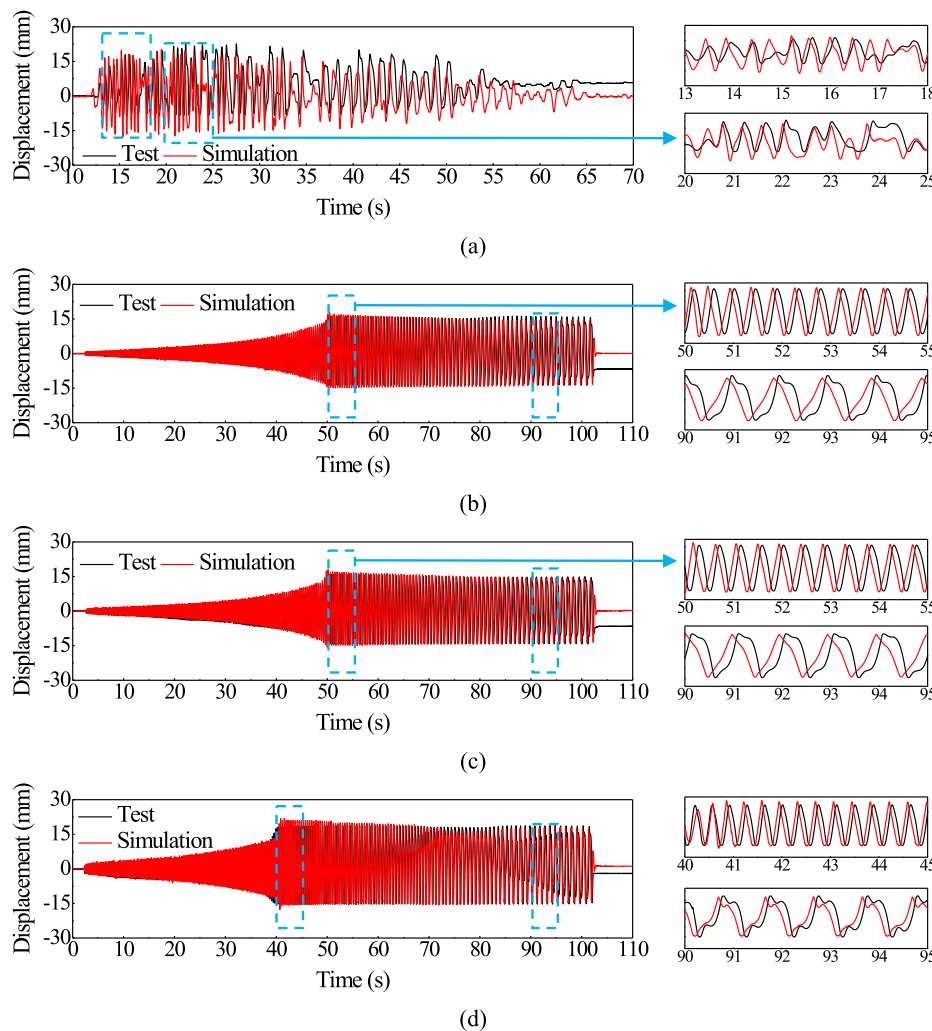


**Fig. 25.** Comparison of displacement time history between simulation and experimental results: (a) 0.405 g (X) & 0.377 g (Y) Random (Run 16), (b) 0.15 g (X) Sweep (Run 18), (c) 0.15 g (X) & 0.15 g (Y) Sweep (Run 22), and (d) 0.25 g (X) Sweep (Run 24).

## Data availability

Data will be made available on request.

## Acknowledgments

The authors acknowledge the financial support from National Natural Science Foundation of China (grant numbers U2239253) and International Joint Research Laboratory of Earthquake Engineering of Tongji University (Grant No. 0200121005/058).

## References

- [1] Devin A, Fanning PJ. Non-structural elements and the dynamic response of buildings: a review. *Eng Struct* 2019;187:242–50.
- [2] Zhou T, Wang X, Liu W, Zhang Z, Ma B, Tan W. Shaking table tests on seismic response of discontinuous suspended ceilings. *J Build Eng* 2021;43:102916.
- [3] Jun S-C, Lee C-H, Bae C-J. Shake table testing of braced and friction-added suspended ceilings and associated numerical study. *Eng Struct* 2022;252:113724.
- [4] Qi L, Kurata M, Ikeda Y. Seismic damage thresholds and design methods for two-elevation continuous ceiling systems. *Eng Struct* 2022;251:113530.
- [5] Soroushian S, Maragakis EM, Jenkins C. Capacity evaluation of suspended ceiling components, Part 1: experimental studies. *J Earthquake Eng* 2015;19(5):784–804.
- [6] ASTM E580/E580M. Standard practice for installation of ceiling suspension systems for acoustical tile and lay-in panels in areas subject to earthquake ground motions. West Conshohocken, PA: ASTM; 2011.
- [7] Yao GC. Seismic performance of direct hung suspended ceiling systems. *J Archit Eng* 2000;6(1):6–11.
- [8] Soroushian S, Rahmanishamsi E, Ryu KP, Maragakis M, Reinhorn AM. Experimental fragility analysis of suspension ceiling systems. *Earthquake Spectra* 2016;32(2):881–908.
- [9] Ryu KP, Reinhorn AM, Filiatrault A. Capacity evaluation of suspended ceiling systems. Buffalo, USA: University at Buffalo; 2014.
- [10] Soroushian S, Rahmanishamsi E, Jenkins C, et al. Fragility analysis of suspended ceiling systems in a full-scale experiment. *J Struct Eng* 2019;145(4):04019005.
- [11] Ryu KP, Reinhorn AM. Analytical study of large-area suspended ceilings. *J Earthquake Eng* 2019;23(4):592–624.
- [12] Takhirov SM, Gilani ASJ, Straight Y. Seismic evaluation of lay-in panel suspended ceilings using static and dynamic and an assessment of the U.S. building code requirements. In: Second ATC & SEI Conference on Improving the Seismic Performance of Existing Buildings and Other Structures, Reston, USA; 2015.
- [13] Soroushian S, Maragakis M, Jenkins C. Capacity evaluation of suspended ceiling-perimeter attachments. *J Struct Eng* 2016;142(2):04015124.
- [14] Dhakal RP, MacRae GA, Pourali A, Paganotti G. Seismic fragility of suspended ceiling systems used in NZ based on component tests. *Bull New Z Soc Earthquake Eng* 2016;49(1):45–63.
- [15] Gilani ASJ, Takhirov SM, Straight Yelena. Evaluation of seismic performance of suspended ceiling systems using dynamic testing and finite element analysis. In: 16th World Conference on Earthquake Engineering, Santiago, Chile; 2017.
- [16] Soroushian S, Maragakis EM, Ryan KL, Sato E, Sasaki T, Okazaki T, et al. Seismic simulation of an integrated ceiling-partition wall-piping system at E-defense. II: evaluation of nonstructural damage and fragilities. *J Struct Eng* 2016;142(2):04015131.
- [17] J502-2-2012. Indoor decoration: suspended ceiling inside. Beijing, China: China Planning Press; 2012 (in Chinese).
- [18] Jun S-C, Lee C-H, Bae C-J, Lee K-J. Shake-table seismic performance evaluation of direct-and indirect-hung suspended ceiling systems. *J Earthquake Eng* 2022;26(9):4833–51.
- [19] Jiang HJ, Wang Y, Kasai K, et al. Shaking table tests on Chinese style suspended ceiling systems. In: 17th World Conference on Earthquake Engineering, Sendai, Japan; 2020.

- [20] Jiang H, Wang Y, He L. Study of seismic performance of Chinese-style single-layer suspended ceiling system by shaking table tests. *Adv Civ Eng* 2021;2021:9861722.
- [21] GB 50010-2010. Code for seismic design of buildings. Beijing, China: Architecture and Building Press; 2016 (in Chinese).
- [22] Wang Y, Jiang H, Huang Y. Study on force-displacement hysteretic model for grid joints and splices of suspended ceiling. *J Tongji Univ (Nat Sci)* 2022;50(3):359–69 (in Chinese).
- [23] Ramhormozian S, Clifton GC, Latour M, MacRae GA. Proposed simplified approach for the seismic analysis of multi-storey moment resisting framed buildings incorporating friction sliders. *Buildings* 2019;9(5):130.
- [24] Pourali A. Seismic performance of suspended ceilings. PhD Dissertation; Christchurch: University of Canterbury; 2017.
- [25] Pourali A, Dhakal RP, MacRae G, Tasligedik AS. Fully floating suspended ceiling system: experimental evaluation of structural feasibility and challenges. *Earthquake Spectra* 2017;33(4):1627–54.